Progress In Electromagnetics Research B, Vol. 35, 369–387, 2011

DESIGN OPTIMIZATION OF TWO SYNCHRONOUS RELUCTANCE MACHINE STRUCTURES WITH MAXIMIZED TORQUE AND POWER FACTOR

S. Tahi[1, *], R. Ibtiouen[2], and M. Bounekhla[3]

[1]Electrical and Industrial Systems Laboratory, USTHB/FEI, Algiers, Algeria

[2]Laboratoire de Recherche en Electrotechnique, Ecole Nationale Polytechnique, Algiers, Algeria

[3]Department of Electronics, Saad Dahleb University Blida, Algeria

Abstract—The subject of this article is to optimize the design of synchronous reluctance machines with massive rotor and multi-flux barrier rotor. The optimization procedure, which aims to improve simultaneously the machines' torque and the power factor, uses the cyclic coordinate method coupled with the magnetostatic finite-element (FE) field solutions. The optimization results regarding these two types of machines, which provide the optimized rotor geometrical dimensions and the influence of the current angle, are discussed.

1. INTRODUCTION

Increasing academic interest has been shown in synchronous reluctance machines (SynRMs) in the last two decades. The main advantage offered is the high-power per volume ratio, which is of interest in embarked applications. Further applications are compressors, centrifuges, and energy storage flywheels [1]. These machines show some advantages based on their ruggedness and construction simplicity. The absence of rotor losses and easy control suggest the possibility of performance and cost effective advantages of the SynRMs over induction motor drives. On the other hand, if the SynRM uses a stator identical to that of the induction machine, then just by changing the punching tools for the rotor geometry, the SynRM can be produced with the same production line [2].

Received 11 September 2011, Accepted 28 October 2011, Scheduled 2 November 2011

* Corresponding author: Slimane Tahi (slim.tahi@gmail.com).

It is well known that the synchronous reluctance motor (salient-pole rotor without field coils) is one of the oldest types of electric motors and has, from time to time, attracted the efforts of a considerable number of investigators. When this type of machines is designed with a massive rotor, they may represent an attractive solution in high speed applications such as flywheel energy storage systems [1, 3, 4]. Moreover, a cage rotor is not required as the induced currents flowing axially in the rotor in the asynchronous operation can generate torque during starting. However, because the saliency ratio cannot be expected to exceed three, these motors are generally characterized by very low power factors or efficiencies [5]. Nevertheless, if the drive system design allows torque ripple reduction, these structures remain attractive if moderate performances are tolerated.

In order that the SynRM has good performances, the rotor should be designed in such a way to reach a high anisotropy ratio, that is for minimum reluctance in the d-axis and maximum reluctance in the q-axis. In fact, the output torque of a current fed synchronous reluctance motor is directly proportional to the difference between the d-axis and q-axis inductances, whereas the maximum power factor is dependent upon the ratio L_d/L_q.

Design improvement can be achieved by introducing flux barriers in the rotor by removing some lamination parts from the rotor core to provide a low reluctance path for d-axis flux and high reluctance path for q-axis flux.

Design development of synchronous reluctance machines performances was the subject of many papers [4, 6, 7]. Recent researches of modern SynRM has focused on structures with axially laminated [8] and multi flux barrier rotors of the transverse-laminated type [9]. The axially laminated rotor can present a high-anisotropy and provide a very high unsaturated saliency ratio [10], but the manufacturing and construction technology of this rotor is expensive and very complicated and presents significant iron loss [7]. Compared to the latter, the flux barrier rotor is easier to manufacture, it can easily be skewed to reduce torque ripple and it has no iron loss problem. The typical way of manufacturing a transverse laminated rotor is to assemble a stack of punched or laser-cut rotor disks with flux paths. A design mechanically more robust transverse laminated rotor structure with dovetail shaped poles without supporting bridges is presented in [11]. Regarding the efficiency, it is shown in [2] that the SynRM can produce about 90%–100% of the induction machine (IM) torque with about 50% lower total losses, at the same stator current, and consequently a higher efficiency of about 5%–8%.

Therefore, owing to the above mentioned advantages, two types

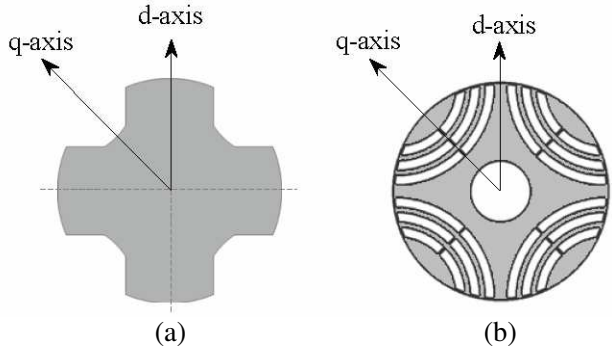

Figure 1. 4-pole SynRMs with (a) massive and (b) transversally laminated flux barriers rotors.

of reluctance rotors are investigated in the present study namely the massive rotor with only cut-outs [Figure 1(a)], and the transverse laminated flux barriers rotor [Figure 1(b)].

This paper describes the design optimization of two SynRM structures using the same stator. In order to determine the optimal machines dimensions and the current angle making a trade-off between the maximum output torque and a high power factor, a cyclic coordinate method coupled with the FEM is applied. For the two studied machines, results regarding the evolution during the optimization process of the design parameters, the maximum output torque and power factor are presented.

2. SYNCHRONOUS RELUCTANCE MOTOR MODELING

In the *d-q* axes reference frame linked to rotor, the phasor diagram of the SynRM in steady state is shown in Figure 2, where the angle φ is the power factor angle and γ is the current space phasor angle.

The electromagnetic torque is given by:

$$T_{dq} = \frac{3}{2} p \left(\psi_d i_q - \psi_q i_d \right) \tag{1}$$

where p is the number of pole pairs, ψ_d, ψ_q, i_d and i_q are the d and q components of the flux linkage and current respectively. The flux linkages are expressed by:

$$\psi_d = L_d i_d \tag{2}$$

$$\psi_q = L_q i_q \tag{3}$$

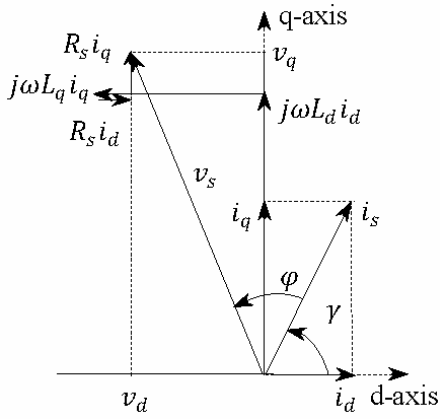

Figure 2. Synchronous reluctance motor phasor diagram expressed in rotor reference frame.

Using the relationship between the flux linkage and the current, Equation (1) can be written as:

$$T_{dq} = \frac{3}{4} p \left(L_d - L_q\right) i_s^2 \sin 2\gamma \tag{4}$$

where i_s is the stator current magnitude.

Neglecting the stator resistance R_s, the power factor as a function of current angle γ for a machine with any saliency ratio $\xi = L_d/L_q$ may be written as:

$$\cos\varphi = \frac{\xi - 1}{\sqrt{\xi^2 \frac{1}{\sin^2\gamma} + \frac{1}{\cos^2\gamma}}} \tag{5}$$

According to Equation (5), the power factor achieves its maximum when the current angle is equal to:

$$\gamma_{\max} = a \tan \sqrt{\xi} \tag{6}$$

and the maximum power factor is:

$$\cos\varphi_{\max} = \frac{\xi - 1}{\xi + 1} \tag{7}$$

The motor power factor versus saliency ratio ξ under maximum power factor scheme is plotted in Figure 3. Note that for machines with a saliency ratio of 7–8, the power factor is near 0.8 which is quite typical of class B induction machine rated about 10 hp [5].

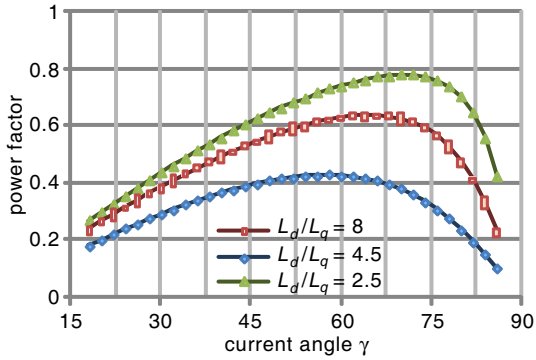

Figure 3. Power factor versus the phasor current angle for different saliency ratios L_d/L_q.

3. FINITE ELEMENT MODELING

A magnetostatic nonlinear 2D finite element package "femm" [12] is employed to investigate the effects of rotor geometrical parameters on the magnetic field distribution. For a given stator current vector and rotor position, the magnetic field is obtained, then the electromagnetic torque and the phases flux linkages are calculated.

In 2D problems, the corresponding Maxwell equation is expressed as:

$$\begin{cases} \frac{\partial}{\partial x}\left(\frac{1}{\mu}\frac{\partial A_z}{\partial x}\right) + \frac{\partial}{\partial y}\left(\frac{1}{\mu}\frac{\partial A_z}{\partial y}\right) = -J_z \\ A_z = 0 \quad \text{on the machine contour} \end{cases} \tag{8}$$

where A_z and J_z are the z components of magnetic vector potential A and the current density J, respectively, and μ is the permeability of the magnetic circuit.

3.1. Torque Calculation from Maxwell's Stress Tensor Method

Methods based on Maxwell's stress tensor are commonly used in the computation of torques for electromagnetic devices when finite element method is employed [13].

The electromagnetic torque is obtained as a surface integral:

$$T_M = \oint_{\Gamma} r \times \sigma dS \tag{9}$$

where σ is Maxwell's stress tensor and S is the integration surface. In the case of a rotating electrical machine, a closed integration surface

that surrounds the rotor in free space is chosen. In a 2D model, where the field is uniform in the axial direction, the surface integral is reduced to a line integral along the airgap. If a circle of radius r is taken as the integration path, the torque equation can then be written as:

$$T_M = \frac{l}{\mu_0} \oint_{\Gamma} r B_t B_n d\Gamma \tag{10}$$

where l is the length of the machine, B_n and B_t are the radial and tangential components of the flux density B.

3.2. Flux Linkages

In Equation (1), the d and q components of the flux linkage are determined from those of stator phases a, b and c. The flux linkage can be calculated from the average vector potential over each winding cross section [14]. For instance, the phase a flux linkage is given by the following expression:

$$\psi_a = \frac{N_{ph} l}{S} \left(\int_{S_1} A_z dS - \int_{S_2} A_z dS \right) \tag{11}$$

where N_{ph} is the number of turns per phase and S is the cross-section of the phase winding region. Subscripts 1 and 2 denote winding sides located in different pole regions.

The actual flux linkages $[\psi_{abc}]$ of the stator three phases (a, b, c) contain harmonics and it is necessary to obtain the fundamental total flux linkages. Assuming that only the 3rd harmonic is dominant, and ignoring higher harmonics, the flux linkage vector in the stator three phases can be written as [15]:

$$[\psi_{abc}] \approx [\psi_{abc1}] + [\psi_{abc3}] \tag{12}$$

The co-phasal 3rd harmonics can be obtained from the actual flux linkages as:

$$\psi_{a3} = \psi_{b3} = \psi_{c3} \approx \frac{1}{3} (\psi_a + \psi_b + \psi_c) \tag{13}$$

With the fundamental flux linkage $[\Psi_{abc1}]$ known and using Park's transformation, the d-q flux linkages are:

$$\psi_d = \frac{2}{3} (\psi_{a1} \cos\gamma + \psi_{b1} \cos(\gamma - 2\pi/3) + \psi_{c1} \cos(\gamma - 4\pi/3)) \tag{14}$$

$$\psi_q = \frac{2}{3} (\psi_{a1} \sin\gamma + \psi_{b1} \sin(\gamma - 2\pi/3) + \psi_{c1} \sin(\gamma - 4\pi/3)) \tag{15}$$

4. DESIGN PROCEDURE

The aim is to optimize two rotor structures of SynRM. Both of the rotors fit in a standard 4 pole — three phase induction machine stator. Main design details of the induction motor are given in Table 1. The magnetization characteristic used for the stator and rotor cores is that of *XC38* mild steel. To add this characteristic in the material library, in the form of *B-H* data points, of the utilized finite element package "femm", the magnetization curve was first approximated by a polynomial with odd powers of the flux density B. Then a sufficient number of *B-H* data points are calculated from the polynomial and entered in the package. From Figure 4, showing the resulting magnetization curve, it can be seen that the *XC38* steel

Table 1. Main data of the SynRM stator.

Item	Value
Rated output power (kW):	3.7
Rated voltage (V):	220/380
Rated current (A):	8
Number of poles:	4
Frequency (Hz):	50
Number of stator slots	36
Outer stator diameter (mm)	190
Inner stator diameter (mm)	122.8
Airgap length (mm)	0.6

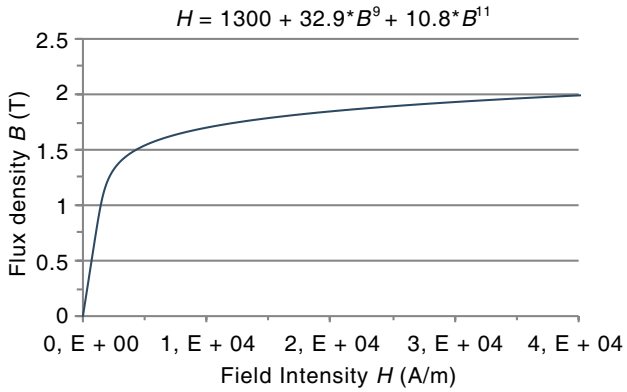

Figure 4. Magnetization curve of the *XC38* steel.

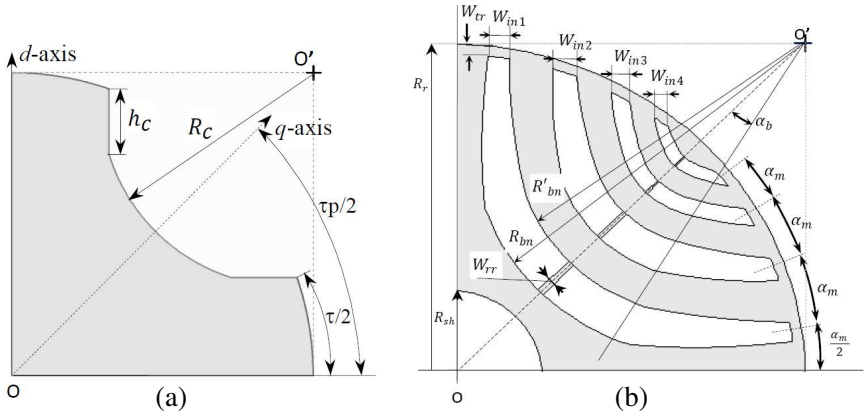

Figure 5. Cross-sectional view of the studied SynRMs: (a) simple salient pole rotor, (b) flux barrier rotor.

has a low permeability compared with other materials.

4.1. Massive Rotor Design

The cross section of the four-pole massive rotor structure investigated is presented in Figure 1(a). The rotor presents a simple and robust structure and it is formed by salient poles and cut-outs without internal flux barriers. The different dimensions defining the rotor structure, which have to be optimized in the design optimization, are as shown in Figure 5(a) where hc, τ and Rc are respectively the rotor cut-out depth, the d-axis pole arc and the q-axis rotor surface cut-out radius. During the optimization process the machine airgap is kept constant and equal to one of the original induction motor (0.6 mm).

4.2. Flux Barrier Rotor Design

Figure 5(b) shows a flux barrier rotor made of standard flat laminations, where the flux barriers are punched in the traditional way in order to obtain the preferred flux path. Thin ribs are left when punching, thus connecting to each other the various rotor segments. It has been shown that the increase in the number of rotor flux barriers does not lead to high gain in the developed torque [7]. To allow for rotor manufacturability easiness, a rotor without cut-off and with four barriers per pole is considered is this study.

A rotor without cut-out is analyzed, having 4 barriers per pole with independent widths (see Figure 5(b)).

The barriers are assumed to have different widths in the design optimization and placed equidistantly around the airgap. Denoting k the number of barriers, the rotor slot pitch can be calculated as follows [16]:

$$\alpha_m = \frac{\frac{\pi}{2p}}{k+1} \tag{16}$$

where p is the number of pole pairs. For $k = 4$ and $p = 2$, we get: $\alpha_m = 0.157\,\text{rd}$ (9° mechanical).

As previously mentioned, to achieve a high saliency ratio, the design of the rotor's barriers must allow the d-axis flux to flow across the whole pole surface and restricts the flow of the q-axis flux. By choosing $k = 4$, the resulting number of iron segments allows the rotor capability to capture the stator magnetomotive force along the d-axis. On the other hand, in order to increase the amount of air along the q-axis, each barrier is given a wider width in the area delimited by the angle $2\alpha_b$, where the both sides of one barrier have different radii R_b and R'_b. (see Figure 5(b)). When $R_b = R'_b$, the barriers have uniform widths.

The parameters of this SynRM to be optimized are as shown in Figure 5(b): the flux barrier widths, W_{in1}, W_{in2}, W_{in3} and W_{in4}, the nth barrier arc radii, R_{bn} and R'_{bn}, and the inner region barriers span angle, α_b. Besides the design variables, there are also a number of parameters with assigned constant values that do not change during the optimization evolution. These parameters are: the airgap length $= 0.6\,\text{mm}$, the tangential rib width $W_{tr} = 0.4\,\text{mm}$, the radial rib width

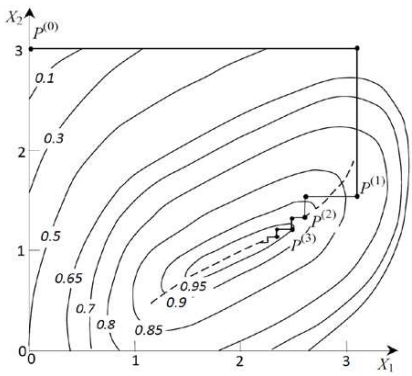

Figure 6. 2-D illustration of the cyclic coordinate method.

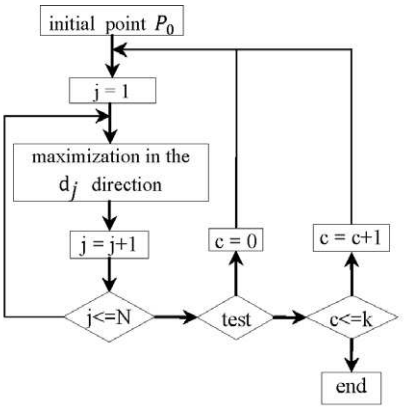

Figure 7. Flowchart of the cyclic coordinate algorithm.

$W_{rr} = 0.4\,\text{mm}$, and the amagnetic shaft radius $R_{sh} = R_r/3$.

In fact, the increase in the thickness of the tangential and radial ribs W_{tr} and W_{rr} decreases significantly the torque production. Thus, these parameters have been fixed to minimal values that ensure mechanical resistance.

4.3. Cyclic Coordinate Method

A cyclic coordinate method [17, 18] using the unknown parameters as the search directions, is applied to maximize the objective function successively along each coordinate. More specifically, the method searches along the directions $d_1, \ldots, d_n$, where d_j is a vector of zeros except for a one at the jth position. Thus, along the search direction d_j, the design variable x_j is changed while all other variables are kept fixed.

This technique is illustrated in Figure 6 through an example of the maximization of an objective function of two variables X_1 and X_2. Starting from the initial point P_0 (X_{10}, X_{20}), the maximization is performed successively along X_1 and X_2 and leads, respectively, to P_1 (X_{11}, X_{20}) and P_2 (X_{11}, X_{21}). The iterative process is repeated until the error test is satisfied. Note that at each iteration k ($k = 1, 2, \ldots, n$), the vectors ($X_1^{(k)}$, $X_2^{(k-1)}$) and ($X_1^{(k)}$, $X_2^{(k)}$) are obtained by performing a line search in the direction of the axes X_1 and X_2, respectively. This in turn defines the point $P^{(k)}$ ($X_1^{(k)}$, $X_2^{(k)}$). Also note that significant progress is made during the first few iterations, whereas much slower progress is made during later iterations

The algorithm shown in Figure 7, estimates the vector parameters

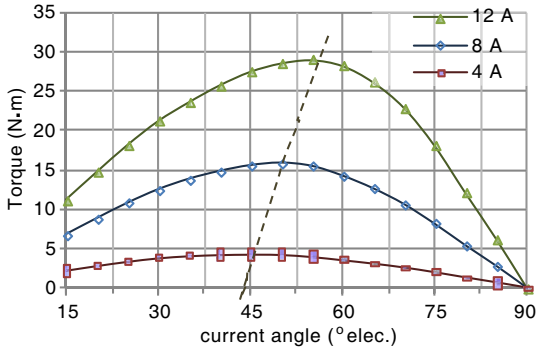

Figure 8. SynRM torque vs. current angle for different stator phase current i_s.

P that maximizes the objective function which increases at each iteration.

Due to self and cross saturation, the difference $(L_d - L_q)$ varies with both the d- and q-axes current of the machine [19]. As a consequence, the maximum output torque does not occur at the theoretical value of $\gamma = 45°$ (elec.) as Equation (4) suggests. The shift of γ to values greater than 45° (elec.) is shown in Figure 8. Moreover, the variation of L_d and L_q affects the saliency ratio and hence the maximum power factor. Thus in this study, an additional parameter is introduced in the optimization process in search for optimum current angle leading to optimal produced torque with high power factor.

In this study, maximum output torque and high power factor are chosen as the optimization criteria. Therefore, numerous requirements corresponding to these two objective functions have to be fulfilled at a time. In this case a multi-objective optimization problem has to be solved. The objective function is then chosen as follows:

$$f = \omega_1 T_{dq} + \omega_2 \cos\varphi_{\max} \tag{17}$$

where T_{dq} and $\cos\varphi_{\max}$ are given by Equations (1) and (7) respectively, ω_1 and ω_2 are weighting factors, which satisfy $\omega_1 + \omega_2 = 1$ with $\omega_1 \geq 0$ and $\omega_2 \geq 0$.

Hence, the objective function may be written as:

$$f = \omega_1 T_{dq}(1 - \omega_1) \cos\varphi_{\max} \tag{18}$$

As stated in Equation (18), the importance of both objectives is adjusted by the weighting factor respect to required performance.

Four parameters for the massive rotor SynRM and eight parameters for the flux barrier rotor are optimized. During simulations, the stator current is set equal to the rated current of the original induction motor.

The design variables are constrained to vary within appropriate intervals such as not to contradict each other and in other hand, to meet

Table 2. Design parameters of the SynRM with massive rotor.

Design parameter	Symbol	Base value	Variable (p.u.)	Lower limit (p.u)	Upper limit (p.u.)
Cut-out depth (mm)	h_c	25	x_1	0	1.2
D-axis pole arc (° mec.)	τ	90	x_2	0.28	0.9
Q-axis rotor surface cut-out radius (mm)	R_c	R_r (60.8)	x_3	0.75	1.7
Current angle (° elec.)	γ	45	x_4	0.78	1.75

Table 3. Design parameters of the SynRM with flux barrier rotor.

Design parameter	Symbol	Base value	variable (p.u.)	Lower limit (p.u.)	Upper limit (p.u.)
Flux barrier width N° 1 (mm)	W_{in1}	6	x_1	0.4	1.2
Flux barrier width N° 2 (mm)	W_{in2}	6	x_2	0.4	1.2
Flux barrier width N° 3 (mm)	W_{in3}	6	x_3	0.4	1.2
Flux barrier width N° 4 (mm)	W_{in4}	6	x_4	0.4	1.2
nth barrier arc radius N° 1 (mm)	R_{bn}	R_r (60.8)	x_5	0.7	0.8
nth barrier arc radius N° 2 (mm)	R'_{bn}	R_r (60.8)	x_6	0.8	1.0
Inner region barriers span angle ($^\circ$ mec.)	α_b	20	x_7	0.1	1.3
Current angle ($^\circ$ elec.)	γ	45	x_8	-0.4	1.6

the mechanical feasibility. In Tables 2 and 3 are presented the upper and lower values of the respective design variables for each studied rotor.

5. OPTIMIZATION RESULTS AND COMMENTARIES

To analyze the importance of each objective function, adjusted by the weighting factor ω_1, and its influence on the optimal design, three cases have been considered in the optimization process, namely:

case 1 for $\omega_1 = 0.75$, case 2 for $\omega_1 = 0.5$ and case 3 for $\omega_1 = 0.25$.

As the used optimization method is a deterministic one, and in order to reach a global optimization, it is appropriate to secure the calculated results regarding the investigated rotors, by using different sets of initial points to check whether the same maximum torque is obtained consistently. In this perspective, in this study, two simulations are then carried out for both the massive rotor and flux barrier rotor structures, respectively. In order to underline the relationship between the calculated torque, using Equation (1), and the

difference ($L_d - L_q$), the d-axis and q-axis inductances are calculated at each iteration from Equations (2) and (3) respectively.

The results of the optimal geometrical dimension of the rotor parameters and current angle after implementing the optimization procedure as described in the previous section are given in the following.

5.1. SynRM with Massive Rotor

When the interpolar cut-out is widened to decrease the q-axis inductance L_q, the pole arc therefore becomes narrower. As a result, the d-axis inductance L_d reduces. Thus large two-axes inductance difference and high saliency ratio cannot be expected for the machine with simple salient pole rotor.

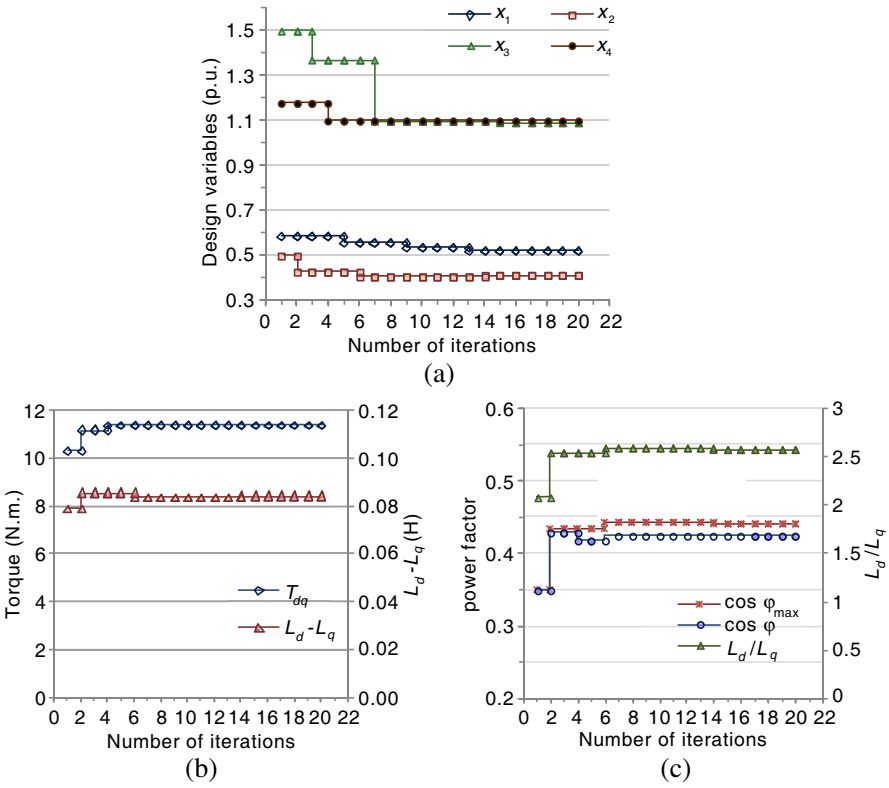

Figure 9. Results of simulation 1, case 1 ($\omega_1 = 0.75$): (a) design variables, (b) torque and d-q inductance difference, (c) power factor and saliency ratio.

The variation of the design parameters, the optimized torque and power factor obtained for $\omega_1 = 0.75$ of the first simulation, are shown in Figures 9(a), 9(b) and 9(c), respectively. It can be observed that the optimized parameters are obtained after 20 iterations. The corresponding developed torque is around 11.4 N·m. This value is also obtained in the two simulations for the three considered cases (see Table 5). Also, it can be noticed that the optimal torque is obtained when the current angle γ_{opt} is around 48–49° (elec.). In fact, when γ varies, the magnetic saturation leads to an increase of the direct axis inductance L_d and also to an increase of L_q though in a lower degree.

Table 4. Initial and optimized values of design variables (p.u.).

	Simulation 1				Simulation 2			
	Initial value	Optimized values			Initial value	Optimized values		
		Case 1	Case 2	Case 3		Case 1	Case 2	Case 3
x_1	0.25	0.52	0.62	0.67	0.85	0.58	0.60	0.72
x_2	0.50	0.41	0.37	0.31	0.72	0.41	0.38	0.32
x_3	1.50	1.09	1.34	0.80	1.13	1.38	1.03	0.94
x_4	1.18	1.1	1.04	0.87	1.24	1.1	1.07	0.88

Table 5. Optimized values of design parameters.

	Simulation 1			Simulation 2		
Design parameter	Case 1	Case 2	Case 3	Case 1	Case 2	Case 3
Cut-out depth (mm)	13	15.5	16.8	14.5	15	18
D-axis pole arc (° mec.)	36.9	33.3	28	36.9	34.2	28.8
Q-axis rotor surface cut-out radius (mm)	66.3	81.5	48.6	83.9	62.6	57.1
Current angle (° elec.)	49.4	46.6	39.3	49.5	48.2	39.6
T_{dq} (N·m)	11.41	11.17	10.40	11.40	11.30	10.51
L_d/L_q	2.6	2.7	3.1	2.6	2.6	3.0
$\cos\varphi$	0.42	0.42	0.42	0.42	0.43	0.41
$\cos\varphi_{\max}$	0.44	0.46	0.52	0.44	0.45	0.50

Hence the difference $(L_d - L_q)$ increases which causes γ_{opt} to exceed the theoretical value of 45° (elec.).

Tables 4 and 5 summarize the obtained optimized values of the design variables for the two simulations. Referring to Table 5, one can verify that approximately the same optimum values of the geometrical design parameters are obtained starting from different initial points. It is noticed that in both simulations, the optimum current angle γ_{opt} is slightly lower when $\omega_1 = 0.25$ compared to the two other cases.

In the other hand, for the three considered values of weighting factor ω_1, the variation of the maximum power factor is not significant. This is due to the fact that, even optimized, this type of rotor structure has limited saliency ratio.

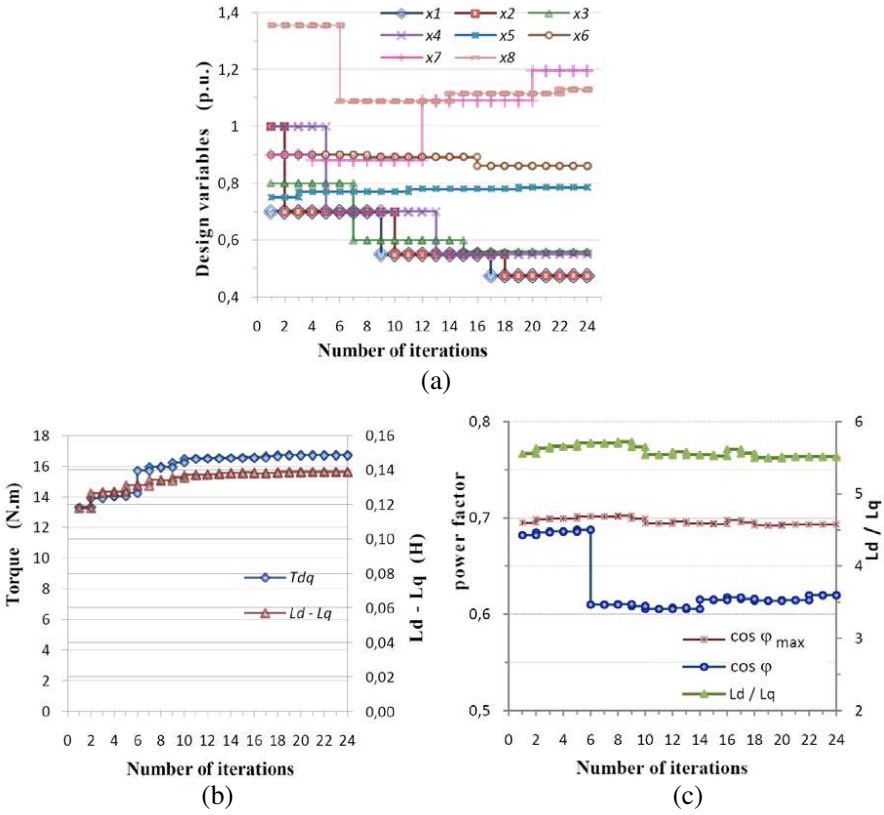

Figure 10. Results of simulation 1, case 1 ($\omega_1 = 0.75$): (a) design variables, (b) torque and *d-q* inductance difference, (c) power factor and saliency ratio.

5.2. SynRM with Flux Barrier Rotor

The variation of the design parameters and the optimized torque and power factor obtained for the first simulation, case 1, are shown in Figures 10(a), 10(b) and 10(c), respectively. It can be observed that the optimized parameters are obtained after 24 iterations. The corresponding developed torque is near 16.5 N·m.

Tables 6 and 7 summarize the obtained optimized values of the design variables for the two carried out simulations. It appears from Table 7 that for both simulations, the optimal values of design parameters compares, for case 1 and case 2, with an optimal current angle γ_{opt} around 52° (elec.) and a maximum power factor of 0.7. Further, in case 3 ($\omega_1 = 0.25$), that is when importance is given to maximum power factor, results show an angle γ_{opt} around 54° (elec.) implying a consistent value of the power factor of 0.65. Actually, when $\omega_1 = 0.25$, the optimization procedure maximizes mainly the saliency ratio ξ, which determines $\cos\varphi_{\max}$ (see Equation (7)), rather than the inductance difference, on which relies the torque production.

Table 6. Initial and optimized values of design variables (p.u.).

	Simulation 1				Simulation 2			
	Initial	Optimized values			Initial	Optimized values		
	value	Case 1	Case 2	Case 3	value	Case 1	Case 2	Case 3
x_1	1	0.475	0.475	0.51	1.2	0.44	0.49	0.53
x_2	1	0.475	0.55	0.56	1	0.39	0.48	0.52
x_3	1	0.56	0.61	0.8	1.1	0.53	0.63	0.82
x_4	0.8	0.55	0.546	0.61	1	0.6	0.58	0.58
x_5	0.75	0.785	0.785	0.78	0.72	0.78	0.787	0.78
x_6	0.9	0.86	0.85	0.84	0.9	0.85	0.853	0.83
x_7	0.9	1.2	1.2	1.25	0.9	1	1.19	1.24
x_8	1.36	1.13	1.16	1.2	1.4	1.14	1.17	1.21

Table 7 also suggests that a reasonable optimal motor design can be chosen when $\omega_1 = 0.5$ owing to the good motor overall performances obtained when the torque and $\cos\varphi_{\max}$ are of equal importance.

Table 7. Optimized values of design parameters.

	Simulation 1			Simulation 2		
Design parameter	Case 1	Case 2	Case 3	Case 1	Case 2	Case 3
Flux barrier width 1 (mm)	2.85	2.85	3.06	2.6	2.9	3.2
Flux barrier width 2 (mm)	2.85	3.3	3.36	2.3	2.9	3.1
Flux barrier width 3 (mm)	3.36	3.66	4.8	3.2	3.8	4.9
Flux barrier width 4 (mm)	3.3	3.27	3.66	3.6	3.5	3.5
nth barrier arc radius 1 (mm)	47.7	47.7	47.4	47.1	47.8	47.4
nth barrier arc radius 2 (mm)	52.3	51.7	51	51.4	51.8	50.46
Inner region barriers span angle (° mec.)	24	24	25	20	23.7	24.8
Current angle (° elec.)	50.9	52.2	54	51.3	52.7	54.6
T_{dq} (N·m)	16.7	16.6	16.1	16.8	16.6	16.1
L_d/L_q	5.5	5.6	5.7	5.42	5.6	5.7
$\cos\varphi$	0.62	0.63	0.65	0.62	0.64	0.65
$\cos\varphi_{\max}$	0.69	0.7	0.7	0.69	0.7	0.7

6. CONCLUSION

The optimization method based on the cyclic coordinate method coupled with FEM, has been applied successfully for the design of synchronous reluctance machine structures with a massive rotor and with a flux barrier rotor for given stator dimensions.

The main objective was to maximize simultaneously the output torque and the power factor. Optimization results showed that for the two investigated SynRMs, a reasonable optimal motor design can be chosen when $\omega_1 = 0.5$ of owing to the good motor overall performances obtained when the torque and $\cos\varphi_{\max}$ are of equal importance.

As a possible improvement of the performances of the studied machines, further investigation would focus on the torque ripple

minimization. Additionally, in the case of the flux barrier rotor, an overall optimization would include the influences of the stator slots on the design of the flux barriers.

REFERENCES

1. Zaïm, M. E., "High-speed solid rotor synchronous reluctance machine design and optimization," *IEEE Transactions on Magnetics*, Vol. 45, No. 3, 1796–1799, 2009.
2. Boglietti, A., A. Cavagnino, M. Pastorelli, and A. Vagati, "Experimental comparison of induction and synchronous reluctance motors performance," *Conference Record of the 2005 Industry Applications Conference, Fortieth IAS Annual Meeting*, Vol. 1, 474–479, 2005.
3. Park, J. D., C. Khalizadeh, and H. Hofmann, "Design and control of high-speed solid-rotor synchronous reluctance drive with three-phase LC filter," *Conference Record of the 2005 Industry Applications Conference, Fortieth IAS Annual Meeting*, Vol. 1, 715–722, 2005.
4. Hofmann, H. and S. R. Sanders, "High-speed synchronous reluctance machine with minimized rotor loss," *IEEE Transactions on Industry Applications*, Vol. 36, No. 2, 531–539, 2000.
5. Matsuo, T. and T. A. Lipo, "Rotor design optimization of synchronous reluctance machine," *IEEE Transactions on Energy Conversion*, Vol. 9, No. 2, 359–365, 1994.
6. Kim, K.-C., J. S. Ahn, S. H. Won, J.-P. Hong, and J. Lee, "A study on the optimal design of SynRM for the high torque and power factor," *IEEE Transactions on Magnetics*, Vol. 43, No. 6, 2543–2545, 2007.
7. Hudák, P., V. Hrabovcová, and P. Rafajdus, "Geometrical dimension influence of multi-barrier rotor on reluctance synchronous motor performances," *International Symposium on Power Electronics, Electrical Drives, Automation and Motion SPEEDAM*, 346–351, 2006.
8. Chalmers, B. J. and L. Musaba, "Design and field-weakening performance of a synchronous reluctance motor with axially laminated rotor," *IEEE Transactions on Industry Applications*, Vol. 34, No. 5, 1035–1041, 1998.
9. Raminosoa, T., I. Rasoanarivo, and F. M. Sargos, "Reluctance network analysis of high power synchronous reluctance motor with saturation and iron losses considerations," *12th International*

Power Electronics and Motion Control Conference, 1052–1057, 2006.

10. Lipo, T. A., A. Vagati, L. Malesani, and T. Fukao, "Synchronous reluctance motors and drives — A new alternative," *Proc. IEEE IAS Annual Meeting, Tutorial Course, Electric Machines Committee*, 1992.
11. Kolehmainen, J., "Synchronous reluctance motor with form blocked rotor," *IEEE Transactions on Energy Conversion*, Vol. 25, No. 2, 450–457, 2010.
12. Meeker, D. C., "Finite element method magnetics, version 4.0.1," (03 December 2006 build), available at: http://femm.foster-miller.net.
13. Popescu, M., "Prediction of the electromagnetic torque in synchronous machines through Maxwell stress harmonic filter (HFT) method," *Electrical Engineering*, Vol. 89, No. 2, 117–125, 2006.
14. Zarko, D., "A systematic approach to optimized design of permanent magnet motors with reduced torque pulsations," Ph.D. Dissertation, University of Wisconsin, Madison, 2004.
15. Kamper, M. J., F. S. van der Merwe, and S. Williamson, "Direct finite element design optimisation of the cageless reluctance synchronous machine," *IEEE Transactions on Energy Conversion*, Vol. 11, No. 3, 547–555, 1996.
16. Moghaddam, R. R., "Synchronous reluctance machine (SynRM) design," M.S. Thesis in Power Electrical Engineering, Royal Institute of Technology (KTH), Stockholm, Sweden, 2007.
17. Bazaraa, M. S., H. D. Sherall, and C. M. Shetty, *Nonlinear Programming Theory and Algorithms*, John Wiley & Sons, Inc., 1993.
18. Zaïm, M. E., K. Dakhouche, and M. Bounekhla, "Design for torque ripple reduction of a three-phase switched reluctance machine," *IEEE Transactions on Magnetics*, Vol. 38, No. 2, 1189–1192, 2002.
19. Haataja, J., "A comparative performance study of four-pole induction motors and synchronous reluctance motor in variable speed drives," Ph.D. Thesis, Lappeenranta University of Technology, 2003.